Tenth International Conference on Computational Fluid Dynamics (ICCFD10), Barcelona,Spain, July 9-13, 2018

ICCFD10-2018-279

Numerical investigations on rectangular and circular synthetic jet impingement

A. Miró*, M. Soria*, C. Moulinec**, J. C. Cajas***, Y. Fournier****
Corresponding author: manel.soria@upc.edu

* Department of Physics, Aerospace Section, Universitat Politècnica de Catalunya, Spain.
** STFC Daresbury Laboratory, Scientific Computing Department, UK.
*** Barcelona Supercomputing Center, Spain.
**** EDF R&D, MFEE, France.

Abstract: Synthetic jets are produced by the oscillatory movement of a membrane inside a cavity, causing fluid to enter and leave through a small orifice. Under certain conditions, the advected vortices are too far to be ingested back and a jet is created. The present study is focused on investigating the differences between the flow of slotted and axisymmetric synthetic jets enclosed between two parallel plates, and impinging into a uniformly heated plate at a certain distance from the actuator orifice. The unsteady three-dimensional Navier-Stokes equations have been solved for Reynolds numbers of 50 and 500 under a jet formation criteria (JFC) of 3 using time-accurate numerical simulations. A detailed model based on an Arbitrary Lagrangian-Eulerian (ALE) formulation is used to account for the movement of the actuator membrane. The flows are noticeably different and are inherently three-dimensional. The axisymmetric configuration presents three different flow regions that have been identified according to the literature: the main vortex ring, the trailing jet and the potential core. On the other hand, the slotted configuration presents two clear vortices that undergo turbulent transition and eventually form the jet. A detailed analysis of the vortex trajectories has shown that the advected vortices on the axisymmetric configuration reach the impingement before their slotted counterparts. Moreover, distributions of turbulent kinetic energy at the expulsion and vortex swirl and shear strength have revealed that the axisymmetric jet is more concentrated near the jet centerline than the slotted jet. For these reasons, at the same jet ejection velocity and actuator geometry, synthetic jet formation on the axisymmetric configuration can occur at higher frequencies than on the slotted configuration.

Keywords: Synthetic Jet Actuator, Numerical Simulation, Vortex, LES, DNS, ALE.

1 Introduction

Synthetic Jet Actuators (SJAs) [1, 2, 3, 4] consist of a cavity with a mechanically moving diaphragm. Its actuation changes the cavity volume periodically, causing external fluid to enter and leave through a small orifice. Under certain conditions, the advected vortices are too far to be ingested back. If so, a train of vortices (and eventually a jet) is created without the addition of mass flow, allowing the transfer of kinetic energy and momentum to a fluid medium without the need of piping systems.

The formation and evolution of SJAs was investigated by Smith and Glezer [5]. The concept of stroke length L_0 was defined as the integral of the stream-wise velocity at the orifice exit u_0 over the ejection part of the cycle, which corresponds to the half of the actuation period τ

$$L_0 = \int_0^{\tau/2} u_0(t)\ dt$$

from which a reference velocity $U_0 = L_0/\tau$ can be defined. It was found out that the evolution of the SJA flow near the orifice is dominated by its time-periodic formation and advection of vortices that roll-up and become part of the jet. It was also observed that their mean trajectory scales with the stroke length. A dimensionless stroke length L_0/d, where d is the orifice diameter, was proposed to be one of the parameters that define the SJA flow [6] and corresponds to the inverse of the Strouhal number. The jet formation criteria (JFC)

$$\text{JFC} = \frac{1}{Sr} = \frac{Re}{Sk^2}$$

introduced by Utturkar and Holman [7, 8], where Sr, Re and Sk are the Strouhal, Reynolds and Stokes numbers based on a time and space averaged velocity $\overline{U}$ at the SJA exit during the expulsion stroke ($\overline{U} = 2U_0$). The difference between this jet formation criteria and the dimensionless stroke length is a constant, as is further discussed in this work. The formation of synthetic jets was analyzed for axisymmetric and two-dimensional configurations and notorious differences were found between them, even though the orifice geometry was similar. The dissimilar fluid flow solutions for the two configurations presented different critical values of a constant K (0.16 and 2 for axisymmetric and two-dimensional configurations respectively) from which the JFC has to be bigger than in order for jet formation to occur. Moreover, as predicted by Utturkar and Holman, experimental investigations of SJA cavity [9] and orifice shape [10, 11] have been found to be influential on the synthetic jet performance.

The flow patterns, namely vortex rings for axisymmetric configurations and vortex dipoles for two-dimensional configurations, resulting from the interaction of the currents entering and leaving the cavity are substantially different and complex. Although many numerical analyses [12, 13] study the two-dimensional (or span-wise periodic) configuration, the axisymmetric configuration is preferred for industrial applications [14, 15, 16]. Many studies have been devoted to analyze the flow morphology of these two configurations, however, to the authors' knowledge, few works have been focused on their comparison.

The flow behavior of axisymmetric impinging synthetic jets has been experimentally analyzed by Greco et. al. [17, 18]. Two different jet morphologies were observed in terms of the dimensionless stroke length. For low dimensionless stroke length or jet formation criteria ($4 \leq L_0/d < 8$ or $1.27 \leq \text{JFC} < 2.55$) the Strouhal number is high and the jet morphology consists of a succession of primary vortex rings, where the impingement is dominated by the vortex ring and results in a larger jet width and lower centerline velocity. On the other hand, at high dimensionless stroke lengths or jet formation criteria ($8 \leq L_0/d < 16$ or $2.55 \leq L_0/d < 5.09$) the Strouhal number is low and the flow is formed by a disconnected primary vortex ring followed by a trailing jet and a region of low turbulence, called potential core. In these flows, the trailing jet, which is formed of multiple vortex rings generated by the Kelvin-Helmholtz instability, becomes the most influential feature of the flow. This behavior and time scales are consistent with what was observed in vortex ring formation for steady jets [19]. In this context, it was observed that, in the case of a vortex ring followed by a trailing jet, the vortex ring reduced its circulation by shedding the excess vorticity into its wake.

The flow patterns of slotted synthetic jets were numerically analyzed by Kral and Donovan [2], where the SJA was successfully implemented as a suction/blowing boundary condition (thus avoiding any representation of the SJA cavity). The evolution and morphology of vortex dipoles was numerically analyzed by Kotapati et al. [12]. They performed span-wise periodic direct numerical simulations (DNS) using a simplified cavity model of the SJA previously analyzed with particle image velocimetry (PIV) by Yao et. al. [20] in the framework of the NASA LaRC Workshop (2004). The main vortex pairs that convect downstream by self-induction were successfully identified along with secondary stream-wise oriented rib-like structures surrounding the main vortex cores. It was found that these structures undergo amplification in the span-wise direction due to vortex stretching and cause the transition to turbulence of the main vortices in the vicinity of the orifice. Thus, a well-developed turbulent jet is eventually formed[12]. Experimental and numerical investigations of the impingement behavior and vortex merging of two-dimensional synthetic jets have been performed by Silva-Llanca et. al. [21, 22]. Different techniques for identifying coherent structures in synthetic jets were compared and the Q-criterion [23] was selected as a vortex presence indicator. Three stages of vortex merging were identified in two-dimensional impinging synthetic jets, in which the expelled vortex slowly merges with the remaining vortex of the previous actuator cycle. This phenomenon was found to be directly proportional to the Reynolds number and inversely proportional to the frequency. Moreover, secondary vortex rings were identified on the impingement plate and were found to have a major role in the heat transfer performance of synthetic jets.

The aforementioned studies in which the synthetic jet impinges into a wall, consider an open configuration and the heated flow is not ingested back inside the actuator; hence the model in which the SJA outlet is assumed to be at a constant temperature is reasonable. Recent numerical studies of opened and enclosed configurations of an axisymmetric synthetic jet, using moving mesh techniques for the membrane description, have been performed by Hatami et. al. [24]. Noticeable differences were found in the flow and heat transfer capabilities between the enclosed and opened configurations. In particular, the advected vortices were found to stretch axially on the enclosed configuration whereas, in the opened configuration, they stretch radially. This has been found to produce more coherent vortices in the opened configuration compared with the enclosed configuration.

The present study, is devoted to a configuration where the jets are enclosed between two parallel plates. Under these circumstances, the external flow interacts with the flow inside the SJA cavity as it is ingested back inside the actuator; thus making the conditions at the actuator outlet hard to estimate. Therefore, a formulation that imposes the movement of the membrane position using Arbitrary Lagrangian-Eulerian (ALE) formulation is proposed to describe a canonical synthetic jet actuator geometry. This allows imposing physically realistic boundary conditions for the momentum and energy equations at the actuator membrane. The other closures that exist in the literature, for example, imposing an inlet velocity [12] or the velocity at the SJA outlet [13], would not be suitable for the present configuration. In addition, the present study is also devoted to understand the impact of the turbulence inside the cavity on the external flow and the impingement.

The aim of the current research is to understand and predict the cooling capabilities of confined synthetic jets; however, the present paper is focused on the description and comparison of the flow features of both SJAs. Hence, the objectives of this paper are: (i) To provide a better understanding of the synthetic jet flow enclosed between two parallel plates for both the span-wise periodic and axisymmetric configurations at Reynolds numbers of 50 and 500 by analyzing the vortices formed in the external and internal flow. (ii) To report the results of a detailed model of the SJA membrane movement using ALE techniques that allow to study the flow and heat transfer mechanism inside the actuator cavity, aiming to provide a better approximation of the flow and temperature at the SJA orifice. (iii) To provide insight on the difference between the flows of the slotted and axisymmetric configurations. Analyses of temperature distributions and Nusselt numbers are left as future work.

This paper is structured as follows: Firstly, the problem is presented followed by a description of the mathematical and numerical models, highlighting the formulation used for the membrane movement and performing a domain and grid sensitivity analysis. Then, the results are examined, starting with a study of the instantaneous flow evolution and an analysis of its temporal spectrum to figure out the dominant frequencies of the flow. This is followed by an investigation of the time and phase averaged flow to illustrate the main structures of the flows and compare two configurations analyzed.

2 Problem Statement and Mathematical Model

The present work is devoted to the analysis of two different actuator configurations: a simplified rectangular actuator in an homogeneous domain in the x_3 direction (henceforth slotted configuration) and a simplified circular actuator (or axisymmetric configuration) as shown in Figure 1. Both jets impinge on a uniformly heated wall located at a orifice-to-surface distance $H/d = 5$, imposed based on the optimal distances for cooling applications [14, 21, 25], causing convective heat transfer from the wall to the jet. For both actuators, the dimensionless actuator cavity width W/d is set to impose a jet formation criteria of 3. The other dimensions of the SJA are selected as in Liu [26], with $b/d = 0.3$ and $B/d = 1.67$. For the slotted configuration, a depth of $D/d = 6$ is considered to allow the full development of the three-dimensional flow.

The Navier-Stokes and energy equations are used to model the flow. Incompressible regime is assumed since the ratio between the Helmholtz frequency of the actuator and the drive frequency os assumed to be less than 0.5 [27, 9]. The present study focuses on situations where the jet velocity is high enough to disregard natural convection, i.e., the Richardson (Ri) number, defined as the ratio of the buoyancy term to the flow shear term, is low enough. Experimental and numerical studies [28] show that buoyancy effects become relevant for Richardson $Ri > 0.01$. Also, for the present work, thermal radiation is neglected. Under

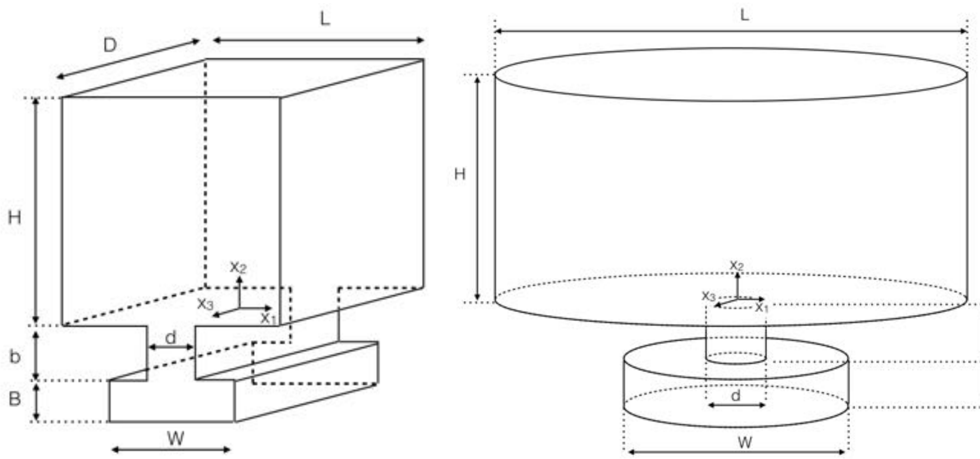

(a) (b)

Figure 1: Geometry of the configurations analyzed (not to scale). (a) Slotted. (b) Axisymmetric.

these assumptions, the incompressible Navier-Stokes equations are

$$\frac{\partial u_j}{\partial x_j} = 0 \tag{1}$$

$$\frac{\partial u_i}{\partial t} + \frac{\partial (u_i u_j)}{\partial x_j} = -\frac{1}{\rho}\frac{\partial p}{\partial x_i} + \frac{\partial}{\partial x_j}\left[\nu\left(\frac{\partial u_i}{\partial x_j} + \frac{\partial u_j}{\partial x_i}\right)\right] \tag{2}$$

$$\frac{\partial T}{\partial t} + \frac{\partial (u_j T)}{\partial x_j} = \frac{\partial}{\partial x_j}\left(\frac{k}{\rho c_p}\frac{\partial T}{\partial x_j}\right) \tag{3}$$

where x_i are the spatial coordinates (or x, y and z), u_i are the cross-stream, stream-wise and span-wise velocity components (or u, v, w), p is the pressure and T is the temperature. ρ is the density, ν is the kinematic viscosity, c_p is the specific heat coefficient at constant pressure and k is the thermal conductivity of the fluid.

The Reynolds number is defined along the standard set by Smith and Glezer [5] as

$$Re = \frac{U_0 d}{\nu}$$

where d is the orifice diameter (see Figure 1) and U_0 is a characteristic velocity defined in terms of the stroke length L_0 as $U_0 = L_0 f_0$, and f_0 is the SJA membrane oscillating frequency. In turn, the stroke length is defined as

$$L_0 = \frac{1}{S_d}\int_0^{\tau/2}\int_{S_d} u_2(x, 0, z, t)dS\ dt \tag{4}$$

where S_d is the actuator outlet surface and τ is the period. The Prandtl number is $Pr = (\rho\nu c_p)/k$ and takes an assumed value of 0.71, whereas the Strouhal number Sr is

$$Sr = \frac{2\pi f_0 d}{U_0}$$

As an alternative to the Strouhal number, some authors [7, 12, 21] define the Stokes number as

$$Sk = \sqrt{\frac{2\pi f_0 d^2}{\nu}}$$

that can also be used to characterize the flow. The relationship between Reynolds, Strouhal and Stokes numbers is given by the jet formation criteria (JFC). For the geometries considered in the present work, if the JFC is lower than an approximated value of 0.16 for the circular geometry and 2 for the span-wise periodic rectangular geometry, the jet is not formed.

In the present work the actuator membrane position is modeled as

$$x_2 = -\delta(x_1, x_3)\cos(2\pi f_0 t) \tag{5}$$

where $\delta(x_1, x_3)$ is a shape function. A mean amplitude can be defined as

$$\overline{A} = \frac{1}{S_W}\int_{S_W} \delta(x_1, x_3)dS$$

where S_W is the surface of the actuator membrane (see Figure 1). Then, the characteristic velocity U_0 can be related to the mean amplitude and the drive frequency $U_0 = 2\overline{A}f_0 S_W/S_d$, thus coupling f_0 and U_0. Therefore, a dimensionless stroke length is obtained by integrating Equation (4) as

$$\frac{L_0}{d} = 2\left(\frac{\overline{A}}{d}\right)\left(\frac{S_W}{S_d}\right) \tag{6}$$

Also, under this definition, the jet formation criteria becomes a purely geometrical parameter.

$$\mathrm{JFC} = \frac{2}{\pi}\left(\frac{\overline{A}}{d}\right)\left(\frac{S_W}{S_d}\right) \tag{7}$$

Therefore, as seen by Smith and Glezer [5], when the motion of the actuator membrane is time-harmonic, the formation parameters of the jet depend only on the amplitude of the actuator, and cannot be varied independently. Moreover, the relationship between JFC and the dimensionless stroke length is $L_0/d = \pi\mathrm{JFC}$. The present work is based on keeping JFC at a constant value of JFC = 3 and focusing on the effects of the Reynolds number. This implies that, according to Equation (7), W/d must differ for both actuators as S_W/S_d is different for each configuration considered. In fact, the actuator width for the slotted configuration must be greater than the actuator width for the axisymmetric configuration in order to achieve JFC = 3.

2.1 Numerical Model

The Reynolds numbers considered are $Re = 50$ and 500. For $Re = 50$, DNS are performed, whereas, for $Re = 500$, simulations are carried out using Large-Eddy Simulations and the filtered equations are used instead

$$\frac{\partial \widetilde{u}_j}{\partial x_j} = 0 \tag{8}$$

$$\frac{\partial \widetilde{u}_i}{\partial t} + \frac{\partial(\widetilde{u}_i\widetilde{u}_j)}{\partial x_j} = -\frac{1}{\rho}\frac{\partial \widetilde{p}}{\partial x_i} + \frac{\partial}{\partial x_j}\left[\nu\left(\frac{\partial \widetilde{u}_i}{\partial x_j} + \frac{\partial \widetilde{u}_j}{\partial x_i}\right)\right] - \frac{1}{\rho}\frac{\partial \mathcal{T}_{ij}}{\partial x_j} \tag{9}$$

$$\frac{\partial \widetilde{T}}{\partial t} + \frac{\partial\left(\widetilde{u}_j\widetilde{T}\right)}{\partial x_j} = \frac{\partial}{\partial x_j}\left(\frac{k}{\rho c_p}\frac{\partial \widetilde{T}}{\partial x_j}\right) - \frac{1}{\rho c_p}\frac{\partial \mathcal{Q}_i}{\partial x_j} \tag{10}$$

where $\widetilde{\cdot}$ denotes the filtered magnitudes. The equations above include the sub-grid scale (SGS) stress tensor

$$\mathcal{T}_{ij} = 2\nu_t\widetilde{S}_{ij} \qquad \widetilde{S}_{ij} = \frac{1}{2}\left(\frac{\partial \widetilde{u}_i}{\partial x_j} + \frac{\partial \widetilde{u}_j}{\partial x_i}\right)$$

which is the deformation tensor of the resolved field and the scalar flux is modeled using a a gradient diffusion approach [29]

$$\mathcal{Q}_i = \rho\frac{\nu_t c_p}{Pr_t}\frac{\partial \widetilde{T}}{\partial x_j} \tag{11}$$

where Pr_t is the turbulent Prandlt number. The present work uses the wall-adapting local eddy viscosity model (WALE) proposed by Nicoud and Ducros [30]

$$\nu_t = (C_w \Delta)^2 \frac{(\mathcal{V}_{ij}\mathcal{V}_{ij})^{3/2}}{\left(\widetilde{S}_{ij}\widetilde{S}_{ij}\right)^{5/2} + (\mathcal{V}_{ij}\mathcal{V}_{ij})^{5/4}} \tag{12}$$

$$\mathcal{V}_{ij} = \frac{1}{2}\left(\widetilde{g}_{ij}^2 + \widetilde{g}_{ji}^2\right) - \frac{1}{3}\delta_{ij}\widetilde{g}_{kk}^2$$

where Δ denotes the cell volume, $C_w = 0.5$ the model constant and δ_{ij} the Kronecker delta. The symbol $\widetilde{g}$ corresponds to the velocity gradient tensor

$$\widetilde{g} = \frac{\partial \widetilde{u}_i}{\partial x_j}$$

and $\widetilde{g}_{ij}^2 = \widetilde{g}_{ik}\widetilde{g}_{kj}$. This SGS model accounts for the effects of the strain and rotation rates as well as an appropriate near wall scaling for the eddy viscosity. From this point onwards, the relevant magnitudes will be expressed in dimensionless form where $\widehat{x}_i = x_i/d$ is the dimensionless spatial coordinates, $\widehat{u}_i = u_i/U_0$ is the dimensionless velocity and $\widehat{T} = (T - T_\infty)/(T_{wall} - T_\infty)$ is the dimensionless temperature where T_{wall} and T_∞ denote the temperature at the heated wall and the bulk temperature, respectively.

For both configurations, non-slip boundary conditions are imposed at the top ($\widehat{x}_2 = H/d$) and bottom ($\widehat{x}_2 = 0$) of the discharge cavity as well as at the actuator walls including the SJA actuator membrane ($\widehat{x}_2 < 0$). Free-flow boundary conditions are prescribed at all the vertical boundaries with $\widehat{x}_2 > 0$. Regarding the energy equation, the cavity top wall is hot ($\widehat{T} = 1$) and the bottom wall is cold ($\widehat{T} = 0$). The lateral boundaries are considered adiabatic ($\partial\widehat{T}/\partial n = 0$). The SJA walls ($\widehat{x}_2 < 0$) are assumed to be cold. Moreover, for the slotted configuration, periodic boundary conditions are set between the front ($\widehat{x}_3 = 0$) and back ($\widehat{x}_3 = D/d$) faces. The SJA membrane movement has been modeled using an ALE formulation with Equation (5) and $\delta(x_1, x_3) = \delta_C \cos(\pi r/W)$, where $r = x_1$ and $r = \sqrt{(x_1^2 + x_3^2)}$ for the slotted and axisymmetric configuration, respectively. In this formulation, δ_C is a scaling parameter used to set a certain value for $\overline{A}$ and W.

Statistically accurate representations of the flow are needed in order to understand the SJA flow. However, the overall system contains very slow temporal scales related with the low velocity zones, despite the intense mixing in the jet vicinity. This results in a very large computational time for the flow to reach statistical stationary conditions (typical numbers are on the order of 200 cycles). For this reason, the flow has been initialized using precursory DNS (for $Re = 50$) or URANS (for $Re = 500$) simulations using the $\mathrm{k} - \omega$ SST [31] model with a large time-step in order to reduce the computational time. With this strategy the statistical stationary state is reached within 20 actuator cycles. Moreover, the initial conditions for the finer meshes are generated from the solution obtained with coarser grids, which in turn reduces the initial transient by 5 cycles. Once the statistical stationary state is reached, the simulations are run for 20 actuator cycles, using the last 15 to obtain relevant time and phase averages of the flow and the Nusselt number.

This work is performed in the framework of collaboration between STFC Daresbury Laboratory, Barcelona Supercomputing Center and the Aerospace Section of Universitat Politècnica de Catalunya, therefore the parallel multi-physics code Alya [32] and the parallel computational fluid dynamics code *Code_Saturne* [33] are used to compute the solution field for the fluid and its thermal interaction with the hot wall. Both codes are designed for large-scale parallel applications [34, 35]. Alya is based on the Finite Element method, using a fractional step approach to solve the pressure-velocity coupling and an explicit fourth-order Runge-Kutta time integration scheme. *Code_Saturne* is based on the Finite Volume method, also using a fractional step to solve the pressure-velocity with a second-order centered scheme as spatial discretization and an implicit second-order Crank-Nicholson time integration scheme.

2.2 Appropriateness of the domain and grid sensitivity analysis

Two similar strategies have been used to design the computational grids: (i) The slotted configuration grid is built by extruding a two-dimensional grid along the x_3 axis for a certain number of planes and a fixed depth of $\widehat{x}_3 = 6$. (ii) The axisymmetric configuration grid is created by the revolution of a two-dimensional grid along the x_2 axis for a certain number of angular divisions. A detail of the computational grids for both configurations is presented in Figure 2. Successive grids have been constructed by multiplying the two-dimensional generator grid. The coarsest grid considered (for $Re = 50$) has $350,000$ control volumes (CV); whereas the finer grids considered (for $Re = 500$) have 4.0 and 5.0 million CV.

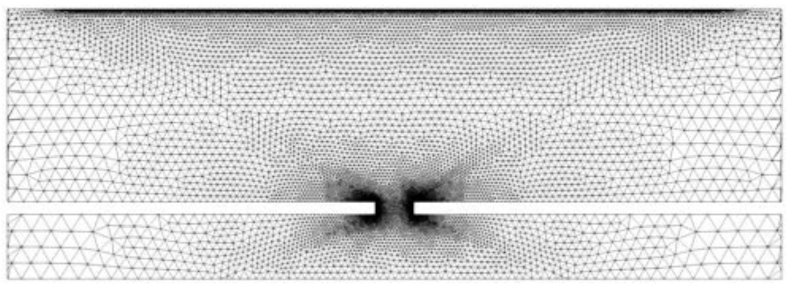

(a)

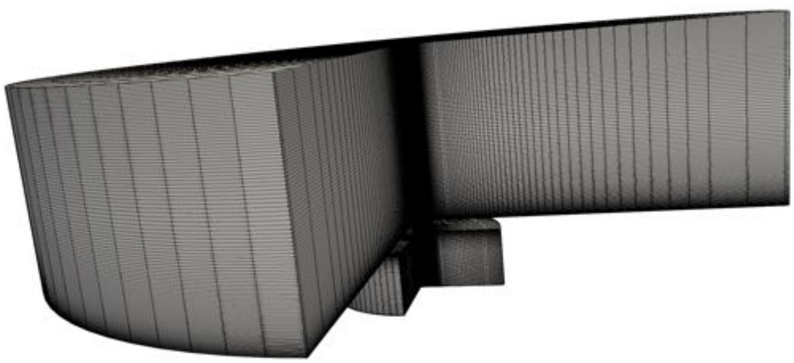

(b)

Figure 2: Detail of the grids' planes, only shown from $\widehat{x}_1 = -10$ to $\widehat{x}_1 = 10$ for clarity. (a) slotted configuration; (b) axisymmetric configuration.

Grid convergence studies have been carried out for each of the Reynolds numbers considered. As an example, Figure 3 shows the grid study for $Re = 500$ and both configurations. The span-wise and phase averaged vertical velocity profiles at different heights are compared for the grids considered, achieving good agreement with minimal differences at the points of maximum and minimum span-wise velocity.

Moreover, for the slotted configuration, the computational domain in the span-wise direction has been designed so as to contain the largest scales of the flow. Span-wise two point correlations are used to verify if the assumed size is correct for all Reynolds numbers considered in this work. They are defined as

$$\mathcal{R}_{ii} = \frac{\overline{u_i'(x_i,t)u_i'(x_i+\delta,t)}}{\overline{u_i'u_i'}} \tag{13}$$

where $\overline{\cdot}$ denotes a time average and $u_i' = u_i - \overline{u}_i$. The values for the two point correlation must tend towards zero for the turbulent cases as they approach the half-size of the domain. Figure 4 illustrates the span-wise two point correlations for $u_3'u_3'$ at $\widehat{x}_1 = 0$ and $\widehat{x}_2 = 2.5$ for all the Reynolds numbers considered in this study. This position has been selected as a representative point where the jet scales have been fully developed. As seen in the figure, all correlations approach zero at the domain half size, thus the domain is wide enough to contain the largest and more energetic scales, except for $Re = 50$. This could indicate the presence of

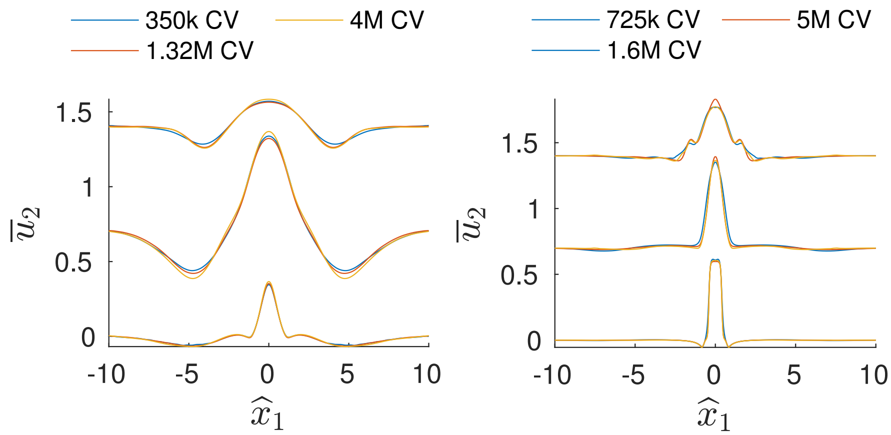

(a) (b)

Figure 3: Span-wise and time-averaged vertical velocity at different heights ($\widehat{x}_2 = 0.5$, $\widehat{x}_2 = 2.5$ and $\widehat{x}_2 = 4.5$, each shifted 0.7 units upwards) for $Re = 500$; blue: coarse grid; red: mid-size grid; yellow: fine grid. (a) Slotted configuration; (b) axisymmetric configuration.

quasi-laminar structures and a larger domain would be needed. However, $W/d = 6$ has been maintained for $Re = 50$ as a good compromise in terms of computational time.

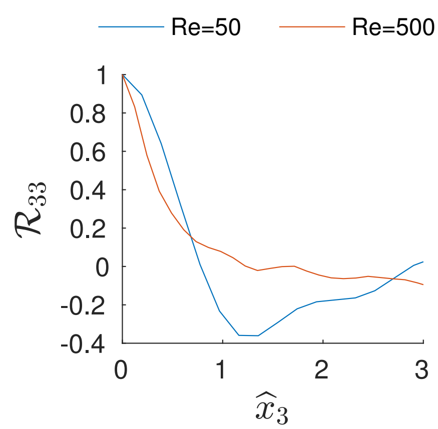

Figure 4: Two point correlation for $u_3'u_3'$ and different Reynolds numbers.

3 Results and Discussion

The flow on a synthetic jet is very complex and its morphology is highly influenced by the JFC and its geometry. Vortices roll up from the actuator lips and move upwards, until the impingement into the top wall is reached.

3.1 Instantaneous Flow

The flow at $Re = 50$ is represented in Figure 5 for a typical instant. The vortical structures have been identified by means of Q-isocontours [36] where Q is the second invariant of the velocity gradient tensor and is defined as

$$Q = -\frac{1}{2}\frac{\partial u_i}{\partial x_j}\frac{\partial u_j}{\partial x_i} \tag{14}$$

The condition $Q > 0$ has been found to be effective in identifying regions of coherent vorticity [22, 23]. The flow is laminar for both configurations at $Re = 50$. While for the slotted configuration is clearly three-dimensional, the axisymmetric flow is almost two-dimensional except for some structures that are generated at the impingement (not visible in this frame). The trailing jet observed for high JFC synthetic jets is not visible as Re is too low and the Kelvin-Helmholtz instability is not triggered.

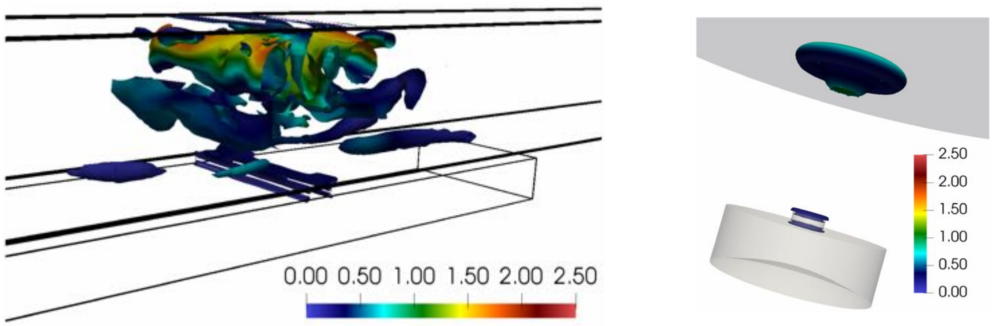

Figure 5: Q-isocontours ($Q = 0.1$) colored by the dimensionless velocity magnitude at $t = \tau/4$ for the slotted (left-hand side) and axisymmetric (right-hand side) configuration at $Re = 50$.

The flow at $Re = 500$ has a more interesting behaviour. Typical instantaneous vortical structures are represented in Figure 6. Four different instants (or phases) are illustrated: Figure 6 (a) and (c) are the maximum expulsion ($t = 0$) and maximum ingestion ($t = \tau/2$) phases, while Figure 6 (b) and (d) are the maximum positive ($t = \tau/4$) and negative ($t = 3\tau/4$) membrane displacement phases. A large amount of vortical structures can be observed in the flow for $Re = 500$, mostly concentrated in the zones near the orifice, both outside and inside the synthetic jet actuator cavity. During the ejection stroke, cold fluid is expelled from the actuator orifice and reaches the top wall at about $t = \tau/4$ (Figure 6 (b)). Then, the heated fluid is taken inside the actuator during the suction stroke ($t = 3\tau/4$), where it is cooled before being ejected again (Figure 6 (d)). Noticeable differences can be observed between the flow of the two configurations. The flow of the axisymmetric configuration starts with a main vortex ring at about $\widehat{x}_2 = 2.5$ (Figure 6 (a), right) being advected downstream from the actuator orifice and reaching the impingement without losing its coherence (Figure 6 (b), right). Along with the main ring, a number of small structures formed by the Kevin-Helmholtz instability can be seen as well as a region of low turbulence in the vicinity of the orifice, the potential core (Figure 6 (b), right). Vortex separation (pinch-off) [19] is observable between the main vortex ring and the trailing jet, although both have reached the impingement and spread through the heated wall during the suction part of the cycle (Figure 6 (c), right). The main vortex ring is persistent enough to be still visible at the start of the next expulsion part of the cycle (Figure 6 (d,a), right). This jet morphology is characteristic of jets with high JFC and is consistent with what has been observed in the literature for continuous and synthetic jets [18, 19, 37].

Regarding the slotted configuration, the vortex dipoles roll-up from the orifice and almost lose all coherence due to the interaction with the smaller structures and the vortex stretching (Figure 6 (a), left). This creates a jet that advects downstream until the impingement is reached (Figure 6 (b), left). During the suction part of the cycle, some of these structures are ingested back inside the actuator cavity (Figure 6 (c), left). Moreover, there is no noticeable potential core as it is seen in the axisymmetric configuration. This jet morphology and behavior are also consistent with what is observed for two- and three-dimensional slotted synthetic jets [12, 22].

Due to the temporal scales associated with the low velocity zones, it is interesting to identify the frequencies related to these zones as they have an impact on the averaged flow statistics. To do so, a set of numerical probes have been located at different zones of the domain and the signal of the independent variables has been recorded during the entire simulation. These numerical probes are located in the following matrix: $\widehat{x}_1 = 0,\ 5, \text{and } 10$, $\widehat{x}_2 = 0,\ 2.5, \text{and } 4.5$ and for each plane in the $\widehat{x}_3$ or angular direction.

The spectrum of the stream-wise velocity of some of these numerical probes is analyzed in Figure 7. As it can be seen, the centerline flow ($x_1 = 0$) is mostly dominated by the periodicity of the ejection and

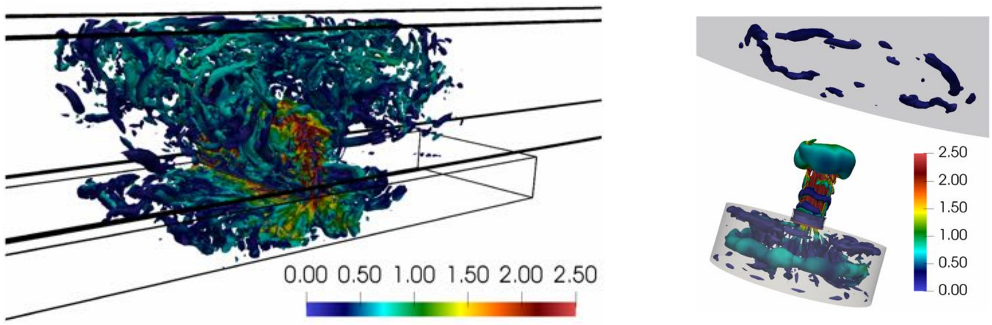

(a)

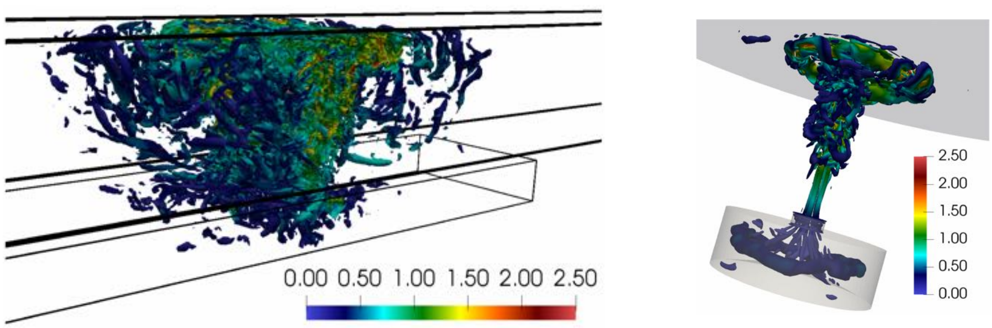

(b)

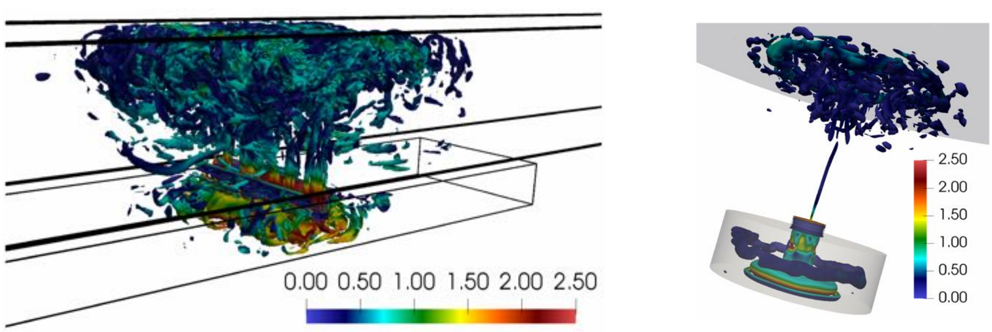

(c)

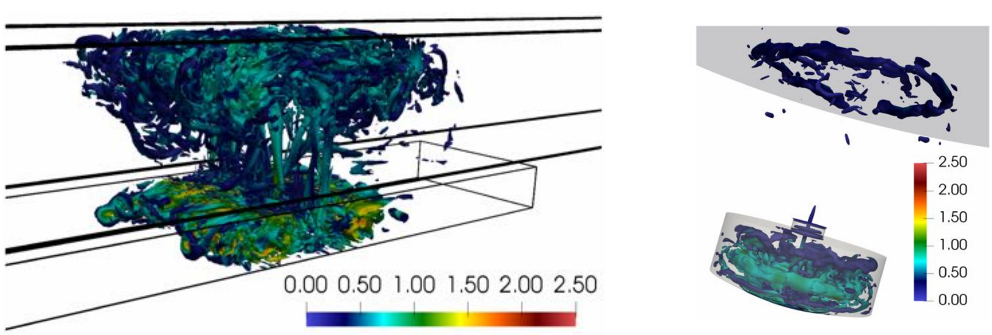

(d)

Figure 6: Q-isocontours ($Q = 1.0$) colored by the dimensionless velocity magnitude at different phase instants for the slotted (left-hand side) and axisymmetric (right-hand side) configuration at $Re = 500$. (a) phase $t = 0$; (b) $t = \tau/4$; (c) $t = \tau/2$; (d) $t = 3\tau/4$.

suction events in both configurations, marked in the figures as driving frequency. When comparing the energy contained in this peak for both configurations, it can be seen that it is higher for the axisymmetric configuration. Notice that in both configurations, the spectra also contain harmonics of the main peak, at frequencies $2f/f_0$, $3f/f_0$ and further for the axisymmetric configuration, corresponding to the vortices created by the Kelvin-Helmholtz instability. The footprint of the cyclic ejection/suction event can still be observed when the flow away from the jet centerline is inspected, yet the energy contained in the peaks is decreased. Notice that the energy contained in the peaks for the axisymmetric configuration away from the centerline are much lower than the energy contained in the slotted configuration. Moreover, a broadband low-frequency signal, also marked in the figures, can be seen for both configurations corresponding to the slow motion of the largest scales of the flow. This peak is centered around $f = 0.0075$ for $Re = 500$, which roughly corresponds to approximately 7 actuator cycles. These frequencies are also related with the vibration frequencies of the larger structures that have been identified in the flow, as it will be later seen. Moreover, as a result of this low-frequency motion, well-converged statistics of the flow far from the jet centerline require a longer time integration of at least a few slow-motion full cycles. In addition, these frequencies are independent of the geometry studied and are mostly influenced by the Re and Sk numbers (or JFC) selected.

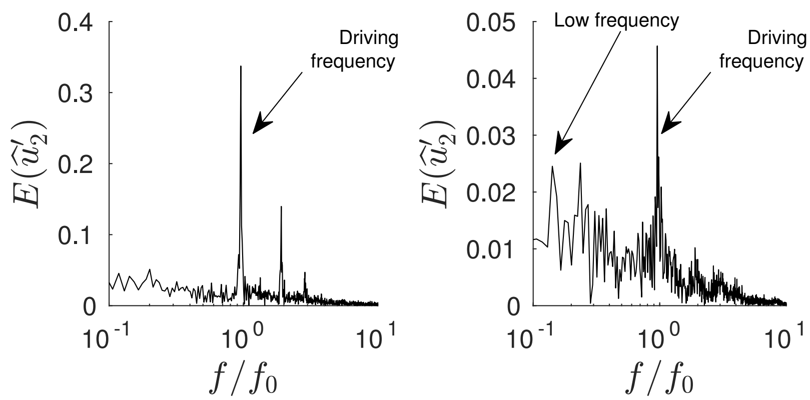

(a)

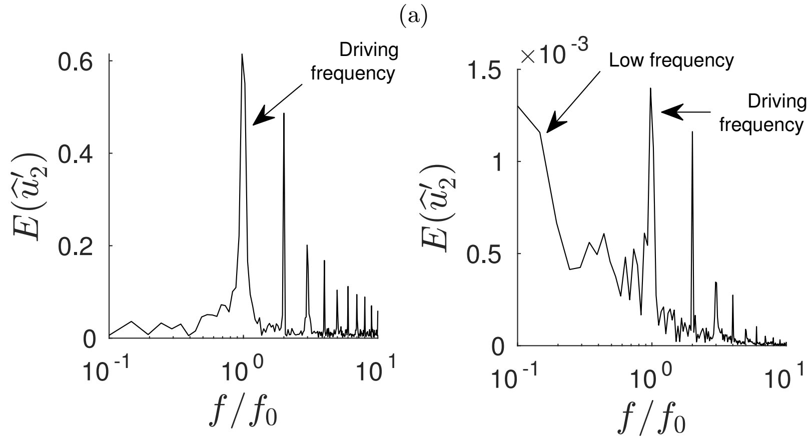

(b)

Figure 7: Energy spectrum of different probes at $Re = 500$ for the stream-wise velocity. Probe locations are: left-hand side $\widehat{x}_1 = 0$, $\widehat{x}_2 = 2.5$; right-hand side $\widehat{x}_1 = 5$, $\widehat{x}_2 = 2.5$. (a) Slotted configuration; (b) axisymmetric configuration.

3.2 Time and Phase Averaged Flow

Time and phase averaged magnitudes are computed by averaging the last 20 actuator cycles in order to obtain time-accurate statistics. The major vortices have been identified and are displayed in Figure 8 for

$Re = 500$ and the two studied configurations. They have been identified using velocity streamlines and with regions where $Q > 0$, which correspond to the shadowed grey areas.

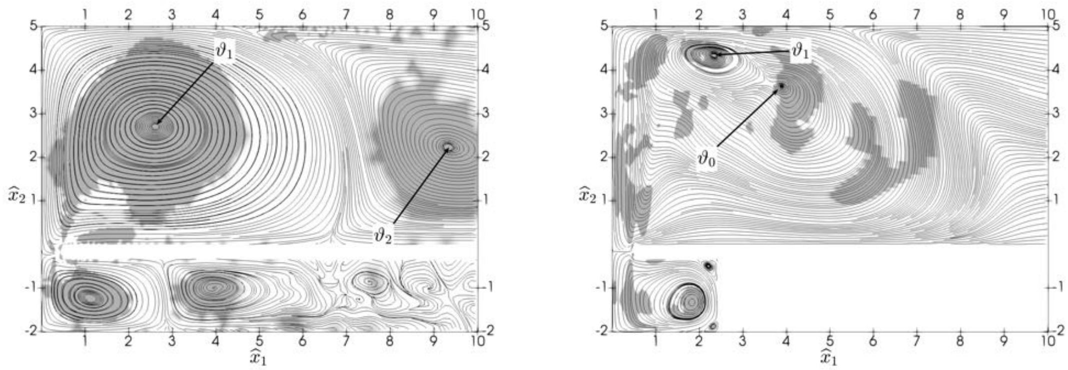

(a) (b)

Figure 8: Time averaged velocity streamlines for $Re = 500$ with the regions with $Q > 0$ highlighted in the background (right-hand side of the computational domain). (a) Slotted configuration; (b) axisymmetric configuration.

In the slotted configuration, two large clock-wise and counter clock-wise vortices (ϑ_1 and ϑ_2 respectively) dominate the external flow field. The former is the result of the coalescence of the vortices ejected from the actuator lips while the latter is characteristic of the enclosed configuration and is not present in the open configurations, e.g., of Silva-Llanca [22]. The axisymmetric configuration also has the clock-wise rotating vortex ϑ_1, albeit it appears much smaller than the slotted counterpart. Another major vortex appears, denoted as ϑ_0, and corresponds to the impinging main vortex of the previous cycle, as it will be further seen. This vortex differs from ϑ_2 in the sense that ϑ_2 appears due to the interaction of the flow far from the jet centerline with the bottom wall. Moreover, the potential core and the trailing jet are visible in the vicinity of the jet centerline in the axisymmetric configuration, but are not present in the slotted configuration. The time-averaged flow inside the SJA is also different for both configurations. While in the slotted configuration, two vortices appear side by side, in the axisymmetric configuration there is one big vortex. This phenomenon is due to the difference in width of the cavities, which is being imposed by the JFC.

McGuinn et. al. [37] presented visualizations of impinging synthetic jets for different JFC on PIV data by using a parameter (s) that allows for an efficient identification of the vortex trajectories. It enables to characterize the strength of a synthetic jet vortex ring and to quantify the swirling and shearing strength of a vortex. It is defined as the negative value of the discriminant of complex eigenvalues of the local velocity gradient tensor [38], i.e.,

$$s = -\frac{1}{4}\left(\left(\frac{\partial \overline{u}_1}{\partial x_1}\right)^2 + \left(\frac{\partial \overline{u}_2}{\partial x_2}\right)^2\right) + \frac{1}{2}\frac{\partial \overline{u}_1}{\partial x_1}\frac{\partial \overline{u}_2}{\partial x_2} - \frac{\partial \overline{u}_1}{\partial x_2}\frac{\partial \overline{u}_2}{\partial x_1} \tag{15}$$

and allows to disregard much of the weaker turbulent vorticity. This parameter has been used in the present work to compare the time averaged flow of both configurations in Figure 9. The difference of the jet morphology for the two configurations studied is again stressed: the slotted configuration has a wide structure that corresponds to the coalescence of the expelled vortices with a wide vortex path, whereas the axisymmetric configuration has narrower vortex path that becomes wider at the impingement. This has been identified due to the higher velocity of the fluid in the trailing jet that impacts upon the vortex and is in good agreement with what has been observed for high JFC synthetic jets [18, 37]. These effects have implications in the jet width as it will be further discussed.

The dynamics of the flow can be better detected when the phase averaged flow is inspected. Figure 10 shows the major vortices, Θ_0 and Θ_1 following the convention set by Silva-Llanca [22], that have been identified for the phase averaged flow using velocity streamlines and highlighting the regions of $Q > 0$. During the ejection stroke (Figure 10 (a), $t = 0$), a vortex rolls-up from the actuator orifice and is advected

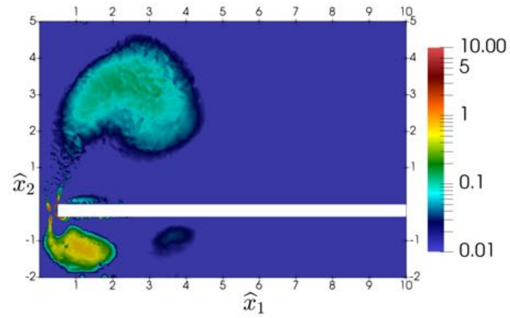

(a)

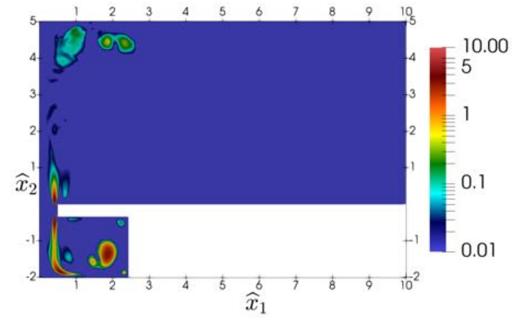

(b)

Figure 9: Time-averaged distributions of the swirl and shear strength parameter s (Equation (15), right-hand side of the computational domain). (a) Slotted configuration; (b) axisymmetric configuration.

downstream on both configurations. Another vortex, Θ_0, is also present and corresponds to the advected vortex of the previous cycle. The advected vortex Θ_1 is seen to interact with Θ_0 in the slotted configuration, whereas it reaches the impingement unperturbed in the axisymmetric configuration (Figure 10 (b), $t = \tau/4$). Notice also the trailing jet area at the vicinity of the jet centerline (Figure 10 (b), right) that reaches the impingement along with the main vortex Θ_1. An additional vortical structure (Θ_s) is created near the impingement point only for the slotted configuration when the suction stroke begins (Figure 10 (c), $t = \tau/2$). It sweeps the surface from left to right until about $\widehat{x}_1 = 6$ and then merges with another structure (Θ_2), which is particular of the enclosed configuration (Figure 10 (d), left). The vortex Θ_s has been identified as the main heat transfer enhancement mechanism for slotted jets in the near wall region in open configurations [14, 22]. Nonetheless, the dynamics of the axisymmetric configuration are significantly different. Following the impingement and during the suction part of the cycle, the vortex Θ_1 sweeps the surface until about $\widehat{x}_1 = 3$, with the effect of the trailing jet mostly seen until about $\widehat{x}_1 = 1$ (Figure 10 (c), right). As the vortex Θ_1 sweeps the impingement surface, it starts to lose coherence and eventually separates from the impingement area. At the start of the next expulsion cycle (Figure 10 (a), $t = 0$), Θ_1 becomes Θ_0 and the dynamics repeat themselves. Vortex dynamics of the axisymmetric configuration depicts a clear contrast with the dynamics of the slotted configuration. In the former, no mixing between Θ_1 and Θ_0 is observed nor the appearance of Θ_2, in contrast to what is observed in the latter.

The spatial distribution of the turbulent kinetic energy (k) at the expulsion stroke ($t = 0$) is plotted in Figure 11. The turbulent kinetic energy (k) is defined as half of the trace of the Reynolds stress tensor

$$k = \frac{1}{2} < u_i' u_i' > \tag{16}$$

where $< \cdot >$ denotes a phase average and $u_i' = u_i - < u_i >$. The different jet morphologies from both configurations are again emphasized. The jet formed in the slotted configuration is clearly of turbulent nature, starting in the region of the orifice at $\widehat{x}_1 = 0.5$, where vortex stretching starts to occur, up to $\widehat{x}_2 = 2$. Also, notice a certain widening as the energy is being transported downstream towards the impingement. On the other hand, the jet formed in the axisymmetric configuration concentrates its turbulent energy on the trailing jet that rises from the actuator lips to the position of the main vortex ring. Moreover, it has lower turbulence levels that are more concentrated in the region of the actuator orifice ($\widehat{x}_1 = 0.5$), in contrast to its slotted counterpart. In addition, a zone of low turbulent kinetic energy near the jet centerline on the axisymmetric configuration that corresponds to the potential core is also observed.

The temporal evolution of the vertical position of the aforementioned Θ_1 vortex is plotted in Figure 12 for both configurations to further analyze the vortex dynamics. It can be seen that, for the axisymmetric configuration, the impingement is reached at $t/\tau \approx 0.4$, whereas for the slotted configuration it occurs at $t/\tau \approx 0.5$. This is due to the vortex Θ_1 being delayed by the interaction with Θ_0, which occurs at about $t/\tau \approx 0.4$ only for the slotted configuration. The vortex Θ_1 remains at $\widehat{x}_2 > 4$ as it sweeps the impingement surface until it loses all its coherence on the axisymmetric configuration, while Θ_1 merges with Θ_0 and

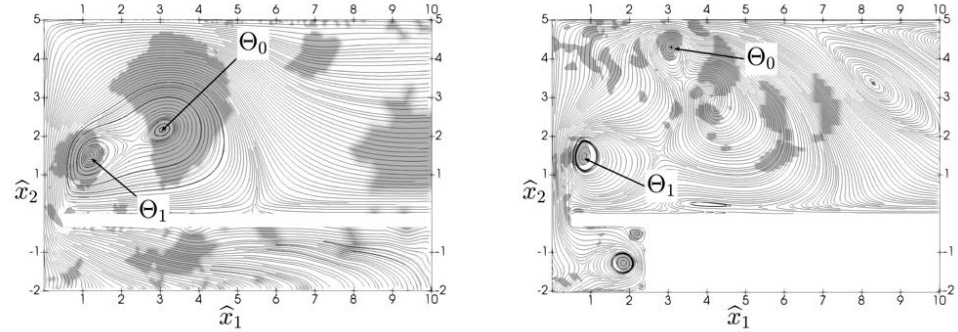

(a)

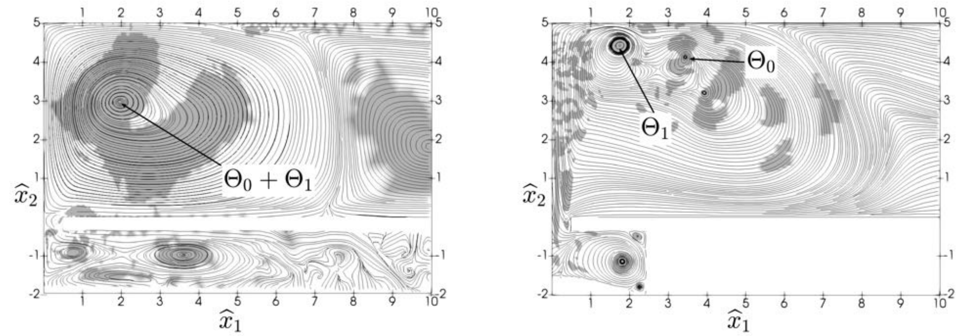

(b)

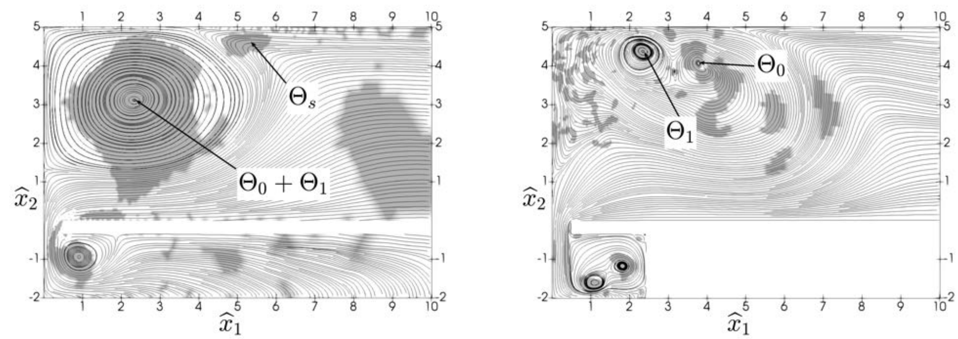

(c)

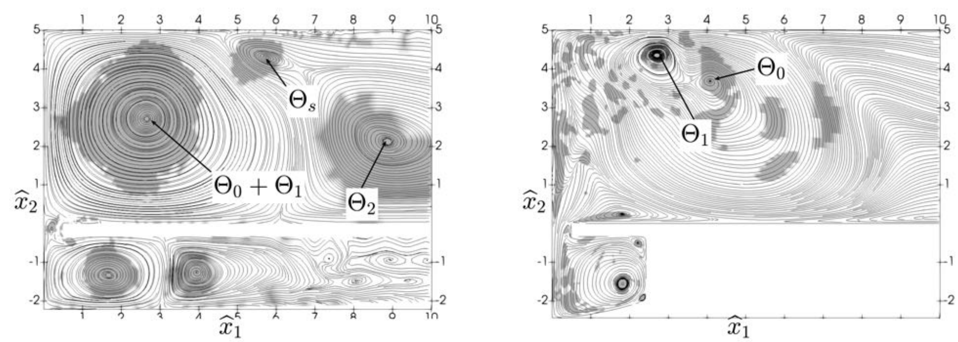

(d)

Figure 10: Phase averaged velocity streamlines for $Re = 500$ with the regions with $Q > 0$ highlighted in the background (right-hand side of the computational domain). Left-hand side: slotted configuration; right-hand side: axisymmetric configuration; (a) phase $t = 0$; (b) $t = \tau/4$; (c) $t = \tau/2$; (d) $t = 3\tau/4$.

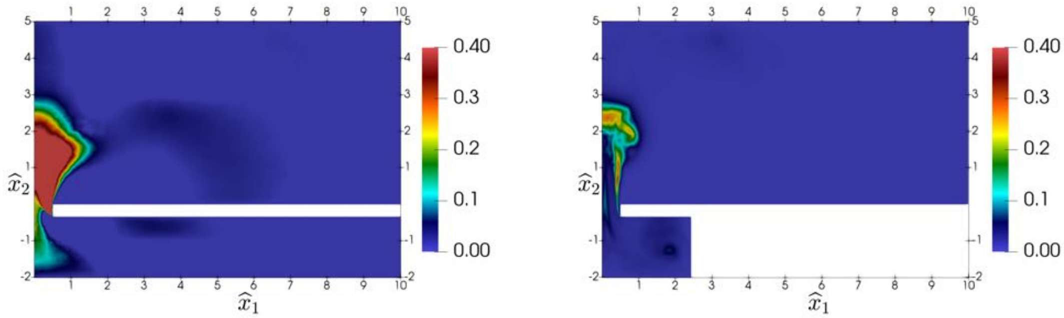

(a)

(b)

Figure 11: Distribution of the turbulent kinetic energy at the expulsion stroke $t = 0$ (right-hand side of the computational domain). (a) Slotted configuration; (b) axisymmetric configuration.

remains at $\widehat{x}_2 \approx 3$ on the slotted configuration. As a result, the vortex Θ_1 in the axisymmetric configuration reaches the impingement surface before the slotted one. This has an impact on the jet formation, which is defined as an outward velocity along the jet axis that corresponds to the generation and escape of a vortex ring [8]. Under this definition and in the light of the data in Figure 12, the reason why the axisymmetric configuration allows lower JFC than the slotted configuration is the aforementioned difference between the velocity of the advected vortices in the two configurations. At the same jet ejection velocity and orifice diameter, the formation of vortex rings of the axisymmetric configuration can occur at higher frequencies than the formation of vortex dipoles of the slotted configuration.

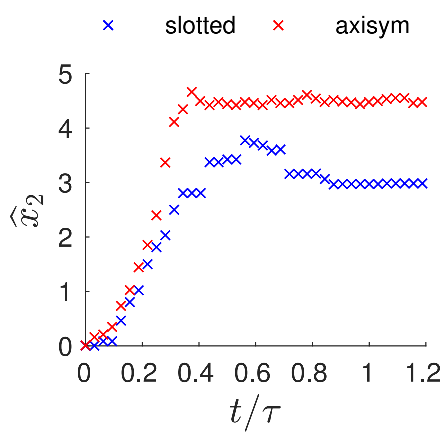

Figure 12: Temporal evolution of the vertical position of the Θ_1 vortex for both configurations.

Another important jet parameter to analyze is the jet half-width or wake. It is defined as the distance from the centerline where the velocity deficit has decayed to one-half of its maximum value and is represented in Figure 13 for both configurations studied. As it can be seen, the slotted configuration jet is wider than its counterpart on the axisymmetric configuration. This is again due to the morphology of the vortex rings and vortex dipoles. In summary: (a) The jet in the axisymmetric configuration is more concentrated on the jet centerline compared with its slotted counterpart, where an interaction between the vortices Θ_0 and Θ_1 is observed. This results in a wider jet on the slotted configuration. (b) The vortices on the axisymmetric configuration reach the impingement before the slotted ones, which results in a more abrupt change of width slope in the jet upper part (as a result of Θ_1 or Θ_s sweeping the impingement surface). (c) The effect of the vortex shedding on the main structures at the vicinity of the orifice and the higher turbulence levels cause a widening of the jet on the slotted configuration, which is not observed in the axisymmetric configuration. (d) The jet width of the slotted configuration increases with Re as a result of an increased mixing between Θ_0 and Θ_1. On the axisymmetric configuration, it is similar for both Re as the main vortex ring does not

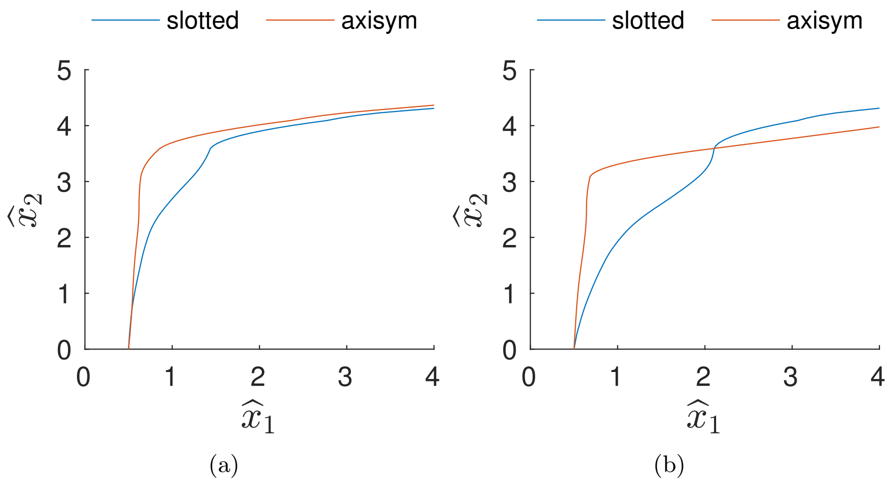

Figure 13: Jet half-width with the domain height for various Reynolds numbers and both configurations. (a) $Re = 50$; (b) $Re = 500$.

lose its coherence until after the impingement. Notice that the zone up to $\widehat{x}_2 = 1$ for $Re = 50$, the jet widths of the slotted and axisymmetric configurations are equal. This is due to laminar vortices being advected from the orifice in both configurations that undergo equal trajectories.

4 Conclusions

Two different synthetic jet configurations, a slotted actuator and an axisymmetric actuator, enclosed between two large parallel plates and impinging into a plate have been studied for $Re = 50$ and 500. At $Re = 50$ DNS of the flow have been performed, while at $Re = 500$ LES have been carried out and the WALE model has been selected as closure for the SGS viscosity. A fixed JFC = 3 has been considered for all of the studied cases. The proposed formulation accounts for the time-periodic movement of the SJA membrane using ALE, therefore, the actuator frequency f_0 and velocity U_0 are coupled and the jet formation criteria becomes a geometrical parameter that depends on the actuator and orifice surfaces. Moreover, this formulation allows for a detailed study both inside and outside the actuator cavity and to obtain an accurate representation of the velocity and temperature at the SJA outlet. A simplified rectangular actuator in an homogeneous domain in the x_3 direction and a simplified axisymmetric actuator have been studied with a orifice to cavity height of $H/d = 5$. The resulting flows are quite complex, and a large number of actuator cycles has to be integrated in order to reach a statistically stationary state. Moreover, it has been found that, for both configurations studied, the far flow field is dominated by frequencies about 7 times lower than the driving frequency, resulting in the overall system having slow temporal scales. In addition, it is confirmed that an ALE model is needed in order to obtain an accurate representation of the SJA cavity for both configurations. The flows studied are inherently three dimensional, even for $Re = 50$, which has an effect on the jet characteristics and the size of the vortices. The differences on the jet morphology of the two studied configurations have been thoroughly identified by means of the Q-criterion and the swirling and shearing strength parameter. The external flow of the slotted configuration is dominated by two major vortices, ϑ_1 and ϑ_2, where the former is the result of the coalescence of the vortices expelled by the actuator and the latter is particular of the enclosed configuration. The axisymmetric configuration also shows the ϑ_1 vortex but also another vortex, ϑ_0, that corresponds to the impinging vortex of the previous cycle. In addition, the external flow of the axisymmetric configuration is also dominated by the trailing jet and the potential core. The vortex dipoles of the slotted configuration have been found to lose coherence early at the roll-up stage, thus creating a highly turbulent jet that advects downstream towards the impingement while it widens on the cross-stream direction. On the other hand, the vortex rings in the axisymmetric configuration are able to maintain their coherence, even after the impingement. The trailing jet contains most of the turbulent energy of the jet; however, it is lower than in the slotted configuration, which results in less jet widening and vortex interaction.

The analysis of the position of the vortices advected from the actuator orifice on both configurations yields that the vortex on the axisymmetric configuration reach the impingement area before their slotted counterparts. This is due to the interaction of the vortex advected from the orifice, Θ_1 with the vortex expelled on the previous cycle Θ_0. Such interaction delays the downstream motion of Θ_1 and occurs in the slotted configuration. This is in good agreement with the axisymmetric SJA having a lower critical JFC than the slotted SJA. These vortex dynamics are expected to have implications in the heat transfer performance of both configurations, which will be the subject of future works.

Acknowledgements

This work has been partially supported by the Spanish Ministry project (MEC) FIS2016-77849-R. The authors thankfully acknoweldge the computer resources at MareNostrum and the technical support provided by Barcelona Supercomputing Center (FI-2016-3-0014 and FI-2017-2-0017). The work has been performed under the project HPC-EUROPA3 (INFRAIA-2016-1-730897), with the support of the EC Research Innovation Action under the H2020 Programme; in particular, the authors gratefully acknowledge the support of Scientific Computing Department of STFC Daresbury Laboratory and the computer resources and technical support provided by EPCC. This work used the ARCHER UK National Supercomputing Service (http://www.archer.ac.uk).

References

[1] A. Glezer and M. Amitay. Synthetic Jets. *Ann. Rev. of Fluid Mech.*, 34:503–529, 2002.

[2] L. Kral, J. Donovan, A. Cain, and A. Cary. Numerical simulation of synthetic jet actuators. 4th Shear Flow Control Conference, 1997.

[3] S. Mallinson, G. Hong, and J. Reizes. Some characteristics of synthetic jets. 30th Fluid Dynamics Conference, 1999.

[4] C. L. Rumsey, T. B. Gatski, W. L. Sellers III, V. N. Vasta, and S. A. Viken. Summary of the 2004 Computational Fluid Dynamics Validation Workshop on Synthetic Jets. *AIAA Journal*, 44:194–207, 2006.

[5] B. L. Smith and A. Glezer. The formation and evolution of synthetic jets. *Phys. of Fluids*, 10(9):2281–2297, 1998.

[6] J. E. Cater and J. Soria. The evolution of round zero-net-mass-flux jets. *J. of Fluid Mech.*, 472:167–200, 2002.

[7] Y. Utturkar, R. Holman, R. Mittal, B. Carroll, M. Sheplak, and L. Cattafesta. A Jet Formation Criterion for Synthetic Jet Actuators. AIAA 2003–0636, 2003.

[8] R. Holman, Y. Utturkar, R. Mittal, B. L. Smith, and L. N. Cattafesta. Formation Criterion for Synthetic Jets. *AIAA Journal*, 43(10):2110–2116, 2005.

[9] M. A. Feero, P. Lavoie, and P. E. Sullivan. Influence of cavity shape on synthetic jet performance. *Sens. and Act. A: Phys.*, 223, 2015.

[10] L. D. Mangate and M. B. Chaudhari. Heat transfer and acoustic study of impinging synthetic jet using diamond and oval shape orifice. *Int. J. of Therm. Sci.*, 89:100–109, 2015.

[11] C.M. Crispo, C.S. Greco, F. Avallone, and G. Cardone. On the flow organization of a chevron synthetic jet. *Exp. Therm. and Fluid Sci.*, 82:136–146, 2017.

[12] R. B. Kotapati, R. Mittal, and L. N. Cattafesta. Numerical study of a transitional synthetic jet in quiescent external flow. *J. of Fluid Mech.*, 581, 2007.

[13] J. P. D'Alencon and L. Silva-Llanca. Two-dimensional numerical analysis of a low-re turbulent impinging synthetic jet. 15th ieee itherm, 2016.

[14] A. Pavlova and M. Amitay. Electronic Cooling Using Synthetic Jet Impingement. *J. of Heat Trans.*, 128(9):897–907, 2006.

[15] M. B. Gillespie, W. Z. Black, C. Rinehart, and A. Glezer. Local Convective Heat Transfer From a Constant Heat Flux Flat Plate Cooled by Synthetic Air Jets. *J. of Heat Trans.*, 128(10):990–1000, 2006.

[16] O. Ghaffari, S. A. Solovitz, M. Ikhlaq, and M. Arik. An investigation into flow and heat transfer of an ultrasonic micro-blower device for electronics cooling applications. *Appl. Therm. Eng.*, 106:881–889, 2016.

[17] C. S. Greco, G. Cardone, and J. Soria. On the behaviour of impinging zero-net-mass-flux jets. *J. of Fluid Mech.*, 810:25–59, 2017.

[18] C. S. Greco, G. Paolillo, A. Ianiro, G. Cardone, and L. Luca. Effects of the stroke length and nozzle-to-plate distance on synthetic jet impingement heat transfer. *Int. J. of Heat and Mass Trans.*, 117:1019–1031, 2018.

[19] M. Gharib, E. Rambod, and K. Shariff. A universal time scale for vortex ring formation. *J. Fluid Mech.*, 360:121–140, 1998.

[20] C. Yao, F. J. Chen, and D. Neuhart. Synthetic Jet Flowfield Database for Computational Fluid Dynamics Validation. *AIAA Journal*, 44:3153–3157, 2006.

[21] L. Silva-Llanca, A. Ortega, and I. Rose. Experimental convective heat transfer in a geometrically large two-dimensional impinging synthetic jet. *Int. J. of Therm. Sci.*, 90, 2015.

[22] L. Silva-Llanca and A. Ortega. Vortex dynamics and mechanisms of heat transfer enhancement in synthetic jet impingement. *Int. J. of Therm. Sci.*, 112:153–164, 2017.

[23] J. C. R. Hunt, A. A. Wray, and P. Moin. Eddies, Streams, and Convergence Zones in Turbulent Flows. Proceedings of the Summer Program 1988, 1989.

[24] M. Hatami, F. Bazdidi-Tehrani, A. Abouata, and A. Mohammadi-Ahmar. Investigation of geometry and dimensionless parameters effects on the flow field and heat transfer of impingement synthetic jets. *Int. J. of Therm. Sci.*, 127:41–52, 2018.

[25] O. Ghaffari, S. A. Solovitz, and M. Arik. An investigation into flow and heat transfer for a slot impinging synthetic jet. *Int. J. of Heat and Mass Trans.*, 100(9):634–645, 2016.

[26] Y. H. Liu, S. Y. Tsai, and C. C. Wang. Effect of driven frequency on flow and heat transfer of an impinging synthetic air jet. *Appl. Therm. Eng.*, 75, 2015.

[27] Q. Gallas. *On the Modeling and Design of Zero-Net Mass Flux Actuators*. University of Florida, 2005.

[28] K. Habibi, S. Amiri, and M. Ashjaee. Study of mixed convection characteristics of confined planar jet impingement using the direct temperature gradient interferometric method. *Int. J. of Therm. Sci.*, 71, 2013.

[29] D. Mira, X. Jiang, C. Moulinec, and D. R. Emerson. Numerical investigation of the effects of fuel variability on the dynamics of syngas impinging jet flames. *Fuel*, 103, 2013.

[30] F. Nicoud and F. Ducros. Subgrid-scale stress modelling based on the square of the velocity gradient tensor. *Flow, Turb. and Comb.*, 62(3):183–200, 1999.

[31] F. R. Menter. Two-equation eddy-viscosity turbulence models for engineering applications. *AIAA journal*, 32:1598–1605, 1994.

[32] BSC-CNS. Alya multiphysics code. [http://www.bsc.es/computer-applications/alya-system], 2014.

[33] F. Archambeau, N. Méchitoua, and M. Sakiz. Code saturne: A finite volume code for the computation of turbulent incompressible flows-industrial applications. *Int. J. on Fin. Vol.*, 1(1), 2004.

[34] M. Vázquez, G. Houzeaux, S. Koric, A. Artigues, J. Aguado-Sierra, R. Arís, D. Mira, H. Calmet, F. Cucchietti, H. Owen, et al. Alya: Multiphysics engineering simulation toward exascale. *J. of Comp. Sci.*, 14:15–27, 2016.

[35] Y. Fournier, J. Bonelle, C. Moulinec, Z. Shang, A.G. Sunderland, and J.C. Uribe. Optimizing Code_Saturne computations on Petascale systems. *Comp. & Fluids*, 45(1):0045–7930, 2011.

[36] J. Jeong and F. Hussain. On the identification of a vortex. *J. of Fluid Mech.*, 285:69–94, 1995.

[37] A. McGuinn, R. Farrelly, T. Persoons, and D. B. Murray. Flow regime characterisation of an impinging axisymmetric synthetic jet. *Exp. Therm. and Fluid Sci.*, 47:241–251, 2013.

[38] R.J. Adrian, K.T. Christensen, and Z.C. Liu. Analysis and interpretation of instantaneous turbulent velocity fields. *Exp. in fluids*, 29(3):275–290, 2000.